

# Engineering Carbon Nanotube Fiber for Real-Time Quantification of Ascorbic Acid Levels in a Live Rat Model of Alzheimer's Disease

Limin Zhang,<sup>†,‡</sup> Fangling Liu,<sup>†,‡</sup> Xuemei Sun,<sup>‡</sup> Guang-feng Wei,<sup>‡</sup> Yang Tian,<sup>\*,†,‡</sup> Zhi-pan Liu,<sup>\*,‡</sup> Rong Huang,<sup>§</sup> Yanyan Yu,<sup>||</sup> and Huisheng Peng<sup>\*,‡</sup>

<sup>†</sup>Shanghai Key Laboratory of Green Chemistry and Chemical Processes, School of Chemistry and Molecular Engineering, East China Normal University, North Zhongshan Road 3663, Shanghai, 200062, P. R. China

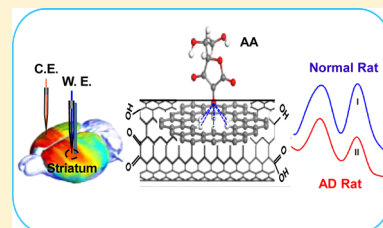
<sup>‡</sup>State Key Laboratory of Molecular Engineering of Polymers, Department of Macromolecular Science and Laboratory of Advanced Materials, and Department of Chemistry, Fudan University, Shanghai, 200433, P. R. China

<sup>§</sup>Key Laboratory of Polar Materials and Devices, Ministry of Education, East China Normal University, Shanghai, 200062, P. R. China

<sup>||</sup>Jiangsu Key Laboratory of New Drug Research and Clinical Pharmacy, Xuzhou Medical College, Xuzhou, Jiangsu 221004, P. R. China

## Supporting Information

**ABSTRACT:** Ascorbic acid (AA) levels are closely correlated with physiological and pathological events in brain diseases, but the mechanism remains unclear, mainly due to the difficulty of accurately analyzing AA levels in live brain. In this study, by engineering tunable defects and oxygen-containing species in carbon nanotubes, a novel aligned carbon nanotube fiber was developed as an accurate microsensor for the ratiometric detection of AA levels in live rat brains with Alzheimer's disease (AD). AA oxidation is greatly facilitated on the fiber surface at a low potential, leading to high sensitivity as well as high selectivity against potential sources of interference in the brain. Additionally, an unexpected, separate peak from the fiber surface remains constant as the AA concentration increases, enabling real-time and ratiometric detection with high accuracy. The results demonstrated that the AA levels were estimated to be  $259 \pm 6 \mu\text{M}$  in cortex,  $264 \pm 20 \mu\text{M}$  in striatum, and  $261 \pm 21 \mu\text{M}$  in hippocampus, respectively, in normal condition. However, the overall AA level was decreased to  $210 \pm 30 \mu\text{M}$  in cortex,  $182 \pm 5 \mu\text{M}$  in striatum, and  $136 \pm 20 \mu\text{M}$  in hippocampus in the rat brain model of AD. To the best of our knowledge, this work is the first to accurately detect AA concentrations in the brains of live animal model of AD.



Ascorbic acid (AA) is a vital antioxidant molecule in the brain,<sup>1–3</sup> playing a major role as reactive oxygen species scavenger and defending the brain against high levels of oxidative stress.<sup>4,5</sup> Thus, alterations to the AA concentration in the brain might have diagnostic value for neurodegenerative diseases. AA also has potentially therapeutic functions in ischemic stroke, Alzheimer's disease, and Parkinson's disease.<sup>6–10</sup> However, the exact mechanisms and functions of AA are still poorly understood due to the lack of accurate and selective methods for *in vivo* AA detection. *In vivo* diagnostics can provide highly detailed information about relevant chemical markers because such tools allow researchers to follow these markers over time under various physiological conditions, which might correlate with brain diseases.<sup>11–13</sup> Electrochemical methods have attracted increasing attention because they allow high spatial resolution and temporal resolution and convenient real-time sensing and, more importantly, prepare carbon fiber electrodes to probe AA levels.<sup>14–25</sup> Because AA oxidation at carbon electrodes exhibits an inner-sphere reaction species,<sup>26</sup> surface functionalization provides an effective bridge to connect nanomaterials to biological systems. In past decades, increasing attention has been focused on the electrochemical activity of AA oxidation at carbon nanotubes (CNTs) with different edge-

plane-like nanotube ends and nanotube sidewalls.<sup>27–32</sup> However, it remains a challenge to carefully design and synthesize functional CNTs aiming at application-specific demands, such as high selectivity and accuracy and long-term stability, for the successful transition of AA biosensors from proof-of-concept studies toward *in vivo* biosensing in live brains.

Recently, CNTs have been assembled into continuous remarkable mechanical and electrical properties.<sup>33–38</sup> In the present study, by engineering tunable defects and oxygen-containing species in CNTs, a novel CNT fiber (CNF) was discovered to greatly facilitate AA oxidation at  $-50 \text{ mV}$  with enhanced current intensity. The low potential for AA oxidation and enhanced current density are beneficial to determine AA levels with high selectivity, avoiding interference from other biological species that exist in brain, as well as producing high sensitivity. More interestingly, a separate peak unexpectedly observed at  $-270 \text{ mV}$  provides a built-in correction to avoid complex environmental effects in the brain. This ratiometric

Received: October 25, 2016

Accepted: January 5, 2017

Published: January 5, 2017

electrochemical sensor provides an accurate and selective method for quantitating AA levels in live brains.

## ■ EXPERIMENTAL SECTION

**Reagents and Chemicals.** Ascorbic acid (AA), dopamine (DA), iron(II) phthalocyanine (FePc),  $\gamma$ -aminobutyric acid (GABA), uric acid (UA), 3,4-dihydroxyphenylacetic acid (DOPAC), L-tyrosine (Tyr), D-tryptophan (Trp), homovanillic acid (HVA), D-(+)-glucose (Glu), 5-hydroxyindole-3-acetic acid (5-HIAA), adenosine triphosphate (ATP), lactate (Lac), 5-hydroxytryptamine (5-HT), ascorbate oxidase (AAox) (Cucurbita species, EC 1.10.3.3), ammonium persulfate (APS), and *N,N*-methylene bis(acrylamide) (BIS) were all purchased from Sigma and used as supplied. Sodium chloride (NaCl), potassium chloride (KCl), monopotassium phosphate ( $\text{KH}_2\text{PO}_4$ ), magnesium chloride ( $\text{MgCl}_2$ ), sodium bicarbonate ( $\text{NaHCO}_3$ ), sodium sulfate ( $\text{Na}_2\text{SO}_4$ ), and calcium chloride ( $\text{CaCl}_2$ ) were purchased from Aladdin-Reagent Company (Shanghai, China). Acrylic acid was obtained from Shanghai Dahe Chemical (Shanghai, China). Chemicals were at least analytical reagent grade and were used without further purification. Artificial cerebrospinal fluid (aCSF) was prepared by mixing NaCl (126 mM), KCl (2.4 mM),  $\text{KH}_2\text{PO}_4$  (0.5 mM),  $\text{MgCl}_2$  (0.85 mM),  $\text{NaHCO}_3$  (27.5 mM),  $\text{Na}_2\text{SO}_4$  (0.5 mM), and  $\text{CaCl}_2$  (1.1 mM) into Milli-Q water, and the solution pH was adjusted to pH 7.4.

**Synthesis of CNF.** The multiwalled carbon nanotube fiber (CNF) was dry-spun from spinnable MWCNT arrays at a rotating rate of 2000 rpm.<sup>33,39,40</sup> The MWCNT arrays were synthesized by chemical vapor deposition (CVD) in a quartz tube furnace with a diameter of 2 in. In a typical synthesis, Fe (1 nm) and  $\text{Al}_2\text{O}_3$  (10 nm) were sequentially deposited on a silicon substrate by electron beam evaporation and used as the catalyst. Ethylene with a flowing rate of 90 sccm was used as carbon source, and a mixture of Ar (400 sccm) and  $\text{H}_2$  (30 sccm) was used as carrying gas. The synthetic reaction was performed at 740 °C for 15 min.

The CNF with more defects (denoted as d-CNF) was prepared through heating treatment at different temperatures ranging from 200 to 400 °C under argon gas. The CNT fibers with oxygen-containing species (denoted as o-CNF) were made through the oxygen microwave plasma at a pressure of 0.1 mbar and flow rate of oxygen gas of 300 sccm (Plasma System 690, PVA Tepla). The oxygen content of CNTs could be tuned by varying the power of oxygen plasma treatment. The powers were ranged from 100 to 400 W for the same time of 15 min to increase the oxygen content in CNT fibers.

**Preparation of CNF Microelectrodes.** A CNF was attached to a copper wire with silver conducting paste. Next, the CNF together with the attached copper wire was carefully inserted into the capillary, in which the CNF was exposed to one open tip of the capillary and Cu wire was extended to the other end of the capillary. Epoxy resin was injected drop-by-drop into the capillary for fixation. Excess epoxy on the CNF was carefully removed with acetone to form microelectrodes. The microelectrodes were thus dried at 100 °C for 1 day, and the exposed CNF was carefully cut down to 4 mm length under microscopy. After the CNF microelectrodes were fabricated, they were kept in a dry and vacuum environment before use. The as-prepared CNF microelectrodes were then sequentially sonicated in acetone, 3 M  $\text{HNO}_3$ , 1.0 M NaOH, and water, each for 3 min, and finally subjected to electrochemical activation. The CNF microelectrodes were electrochemically

pretreated in 0.1 M NaOH with +1.5 V for 100 s. The CNF microelectrodes were further electrochemically treated in 0.5 M  $\text{H}_2\text{SO}_4$  with cyclic voltammetry within a potential range from -1.0 to +1.0 V at a scan rate of 0.1 V  $\text{s}^{-1}$  until a stable cyclic voltammogram was obtained. The fabricated microelectrode was denoted as e-CNF microelectrode hereafter. All potentials in the electrochemical measurement mentioned in this Article were obtained using Ag/AgCl (saturated KCl) as reference electrode. The differential pulse voltammetry (potential step, 4 mV; modulation amplitude, 50 mV; pulse width, 0.05 s; pulse period, 0.4 s) was used to detect AA.

**Apparatus and Measurements.** Electrochemical measurements were performed on a computer-controlled electrochemical analyzer (CHI 832, CHI instrument). The carbon fiber or CNF was used as working electrode, and a platinum wire served as counter electrode. Scanning electron microscopy (SEM, Hitachi S4300-F microscope, Japan) and transmission electron microscopy (TEM JEOL JEM-2100F operated at 200 kV) were employed for characterization of CNFs before and after electrochemical treatments. X-ray photoelectron spectroscopy (XPS, AXIS Ultra DLD, Japan) equipped with an Al  $K\alpha$  (1486.6 eV photons) was used to characterize the CNF. Raman measurements were made on a Renishaw inVia Reflex spectrometer with laser wavelength of 512 nm. Fourier transform infrared spectra were obtained from a Thermofisher NEXUS 470 spectrometer using KBr as the pelletizing material. The morphology of the CNFs was observed by field emission scanning electron microscopy (FE-SEM) on a Hitachi S-4800 SEM. HRTEM observations were performed using a field emission transmission electron microscopy (FE-TEM) on a JEM-2100F operated at 200 kV. In order to avoid the beam damage on the MWCNTs, a very low electron dose was used during the observation. In this paper, error bar represents the standard deviation (S.D.) from three independent assays.

## ■ METHODS

**Periodic Continuum Solvation Model Based on the Modified Poisson-Boltzmann Equation (DFT/CM-MPB) Calculation Details.** All DFT calculations were performed using the SIESTA package with numerical atomic orbital basis sets and Troullier-Martins normconserving pseudopotentials.<sup>41,42</sup> The exchange-correlation functional utilized was at the generalized gradient approximation level, known as GGA-PBES4. The optimized double- $\zeta$  plus (DZP) polarization basis set with extra diffuse function was employed. The orbital-confining cutoff was determined from an energy shift of 0.010 eV. The energy cutoff for the real space grid used to represent the density was set as 250 Ry. The Monkhorst-Pack k-point mesh was utilized for first Brillouin zone integrations. In this work, a (1 × 1 × 1) k-point was applied for the surface adsorption structures and the free energy profile calculations on single-layer graphene sheets (the unit cell size: 17.1 Å × 17.3 Å × 25.0 Å). The Quasi-Newton Broyden method was employed for geometry relaxation until the maximal forces on each relaxed atom were less than 0.05 eV/Å. To correct the zero-point energy (ZPE), the vibrational frequency calculations were performed via the finite-difference approach. The AA oxidation at the solid/liquid interface has been modeled using a periodic continuum solvation model based on the modified Poisson-Boltzmann equation (CM-MPB), which can take into account the long-range electrostatic interaction due to solvation. In this method, we introduce a large vacuum region along the Z axis that separates two adjacent slabs. In the middle of the vacuum

region, we define a potential zero plane as the boundary condition for the integration of the Poisson-Boltzmann equation, which can be solved via the finite-difference multigrid method. The periodic DFT/CM-MPB method has been utilized in our previous work on electro-/photocatalysis, and the detail of the implementation of the method is also described therein.<sup>41,42</sup>

For reactions involving the release of proton and electron, the reaction energy can be computed by referencing to the normal hydrogen electrode (SHE) in a manner proposed by the Bockris<sup>43</sup> and Nørskov groups.<sup>44</sup> This is governed by  $G_{\text{proton+electron}} = G(1/2\text{H}_2) - neU$  where  $e$  represents the transfer electron,  $n$  means the number of electrons, and  $U$  is the electrochemical potential vs SHE. At a pH different from 0, we can correct for the free energy of  $\text{H}^+$  ions by the concentration dependence of the entropy:  $\Delta G_{\text{pH}} = -kT \cdot \ln [\text{H}^+]$ .

**In Vivo Experiments.** The animal model of Alzheimer's disease (AD) was established according to a previous report (as described in the Supporting Information).<sup>45</sup> All procedures involving animals were conducted with approval of the Animal Ethics Committee in Xuzhou Medical College, China. Male Wistar normal rats (100–120 g) were purchased from Shanghai Yisen Biotechnology Co., Ltd., China. Then, the rats (200–250 g) were used for in vivo experiments and anesthetized with chloral hydrate (initial dose of 300 mg kg<sup>-1</sup> (i. p.) with additional doses of 50 mg kg<sup>-1</sup> (i. p.)) as needed to maintain anesthesia and wrapped in a homeothermic blanket (Beijing Tide-Gen Biotechnology Development Center). The rats were placed in a stereotaxic frame (Beijing Tide-Gen Biotechnology Development Center) with the incisor bar set at 5 mm above the interaural line and appropriately placed holes were drilled through the skull. The e-CNF microelectrodes were implanted in left striatum of rat brain model of AD (AP = 0 mm, L = 2.5 mm anterior to bregma, and V = 7.0 mm from the surface of skull). For the investigation for those rat brains with global cerebral ischemia, the e-CNF microelectrodes were implanted in different regions in rat brain of the left striatum (AP = 0 mm, L = 2.5 mm anterior to bregma, and V = 7.0 mm from the surface of skull), the cortex (AP = 0.2 mm, L = 5.6 mm from bregma, V = 3.0 mm from the surface of skull), and the dorsal hippocampus (AP = 5.0 mm, L = 5.0 mm from bregma, V = 2.5 mm from the surface of the skull), according to standard stereotaxic procedures. Another 2 mm plastic cannula was located ~5 mm away from the working electrode, in which reference and counter electrodes were introduced. Throughout the operation, supplements of chloral hydrate (100 mg/kg) were given as required and the body temperature of the animals was maintained at 37 °C using a heating pad. Differential pulse voltammetry (DPV) was employed for in vivo voltammetric measurements of AA in rat brain. In order to confirm the anodic peak observed at -0.05 V vs Ag/AgCl in rat brain ascribed to AA, a fine silicon capillary (i.d. 75 μm) was in parallel combined with e-CNF microelectrode under a microscope with the outlet of the capillary ~400 μm higher than the tip of microelectrode and a 80–100 μm space between the capillary and the microelectrode. The capillary was implanted into the striatum together with the e-CNF microelectrode and was employed to exogenously infuse the solution of AAox into the brain. The solution was delivered from gas-impermeable syringes and pumped through tetrafluoroethylene hexafluoropropene (FEP) tubing by a microinjection pump (CMA 100, CMA Microdialysis AB, Stockholm, Sweden).

**Cerebral Ischemia/Reperfusion Models.** In the two-vessel occlusion ischemia and reperfusion models, the bilateral common carotid arteries were ligated and/or released with the methods reported previously.<sup>46,47</sup> After midline cervical incision, the bilateral common carotid arteries were first isolated. Subsequently, the atlanto-occipital membrane was exposed from the left side by retraction of the trachea and esophagus to the right. The basilar artery was occluded by a vascular clip (0.2 mm diameter; stainless steel), with a tapered blade tip. After the cessation of blood flow in the basilar artery was visually confirmed, both common carotid arteries were occluded using two Yasargil miniclips, and the clips were then removed for 30 min of reperfusion. The duration of the surgical procedure to the application of the final clip was usually 60 min. Ischemic duration was measured from the application of the last clip to the left common carotid artery.

## RESULTS AND DISCUSSION

As shown in Figure 1A, a CNF was constructed of CNT bundles with a uniform diameter of ~10 μm. The diameter can be repeated through strictly controlling the sheet width at 1 cm and the helical angle at 30°. The end of the CNF contains abundant CNT tips with a multiwalled structure (Figure 1B).

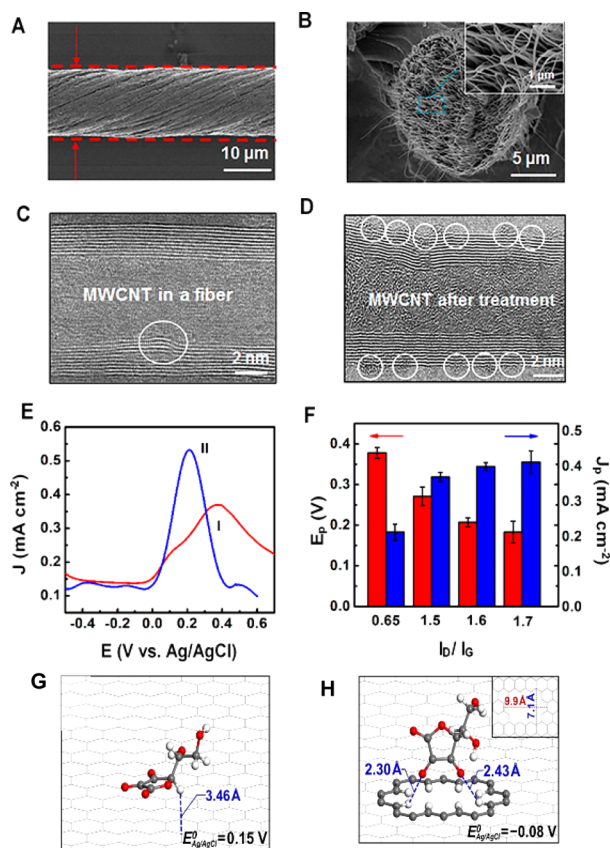


**Figure 1.** SEM images of a CNF from a side (A) and end view (B). (C) STEM image of the MWCNT in a CNF. (D) STEM image of MWCNT in a CNF after heating at 200 °C. (E) Comparison of differential pulse voltammograms (DPVs) obtained at (I) CNF and (II) d-CNF-3 microelectrodes. (F)  $E_p$  (peak potential of AA oxidation, red column) and  $J_p$  (blue column) of the AA oxidation peaks obtained from as-prepared CNF, d-CNF-1, d-CNF-2, and d-CNF-3, respectively. The adsorption structure of dhAA on perfect (G) and defect-containing graphene sheets (H).

The MWCNTs in CNF exhibits clean and uniform structure, and only a little amorphous carbon content remained at the MWCNT (Figure S1). Compared with carbon fiber, the CNF possesses a higher electrocatalytic activity for  $K_3Fe(CN)_6$  redox, with a lower  $|E_{3/4} - E_{1/4}|$  (i.e., 79 mV) and a much higher current density (Figure S2A). However, for AA molecule, an ill-defined cyclic voltammogram was observed with high overpotentials at the CNF microelectrode (Figure S2B) because AA is an inner-sphere reaction species in which the electron-transfer kinetics are highly sensitive toward the electrode surface. Although the existence of defects and functional groups in CNTs has been proposed to be important for AA oxidation,<sup>35,48</sup> it has not yet been verified due to the technical difficulties in controlling the nanostructure and surface modification of CNTs.

Here, three types of CNFs with different degrees of defects were synthesized at different temperatures (denoted as d-CNF-1 at 200 °C, d-CNF-2 at 300 °C, and d-CNF-3 at 400 °C).<sup>49</sup> The defect levels were tracked by the intensity ratio between the D-band at  $\sim 1350\text{ cm}^{-1}$  and the G-band at  $\sim 1580\text{ cm}^{-1}$  ( $I_D/I_G$ ) using Raman spectroscopy. The  $I_D/I_G$  value dramatically increased from the initial 0.65 to 1.5 after heating at 200 °C, indicating the production of a number of defects (Figure S3).<sup>48</sup> The  $I_D/I_G$  values were further enhanced to 1.6 and 1.7, indicating more defects, as the temperature increased to 300 and 400 °C, respectively. The generated defects were further characterized by TEM. As demonstrated in Figure 1C, the as-prepared MWCNTs were almost free of defects, accompanied by some bending and torsion produced during spinning (white solid ellipses). In contrast, the surfaces of MWCNTs in d-CNF-1 became rougher (Figure 1D), and the sidewalls of the MWCNTs were more bent and twisted after the heat treatment. Furthermore, many deep defects in the sidewall were unambiguously observed. Similar and even more bent and twisted structures and defects were present in the other two types of d-CNFs (Figure S4).

Next, the impact of the defects on the electrochemical kinetics of AA oxidation was studied. As shown in Figure 1E, AA was oxidized with a high overpotential of 378 mV in aCSF solution. This sluggish electron transfer kinetic value might be explained by the inactivated surface of the CNF. In contrast, the overpotential for AA oxidation was reduced by 107 mV at the d-CNF-1 microelectrode, and the peak anodic current density ( $J_p$ ) was also increased by 74%. Moreover, the oxidation potential for AA was further decreased by 171 and 205 mV at the d-CNF-2 and d-CNF-3 microelectrodes, and the corresponding  $J_p$  values were increased by 88% and 93%, respectively (Figure 1F). Therefore, the electron-transfer kinetics of AA oxidation were markedly enhanced at the d-CNFs with more defect.

We further utilized the periodic continuum solvation model based on modified Poisson-Boltzmann electrostatics in combination with density functional theory (DFT) calculations (DFT/CM-MPB)<sup>32,33</sup> to study the AA oxidation process ( $C_6H_8O_6 \rightarrow C_6H_6O_6 + 2H^+ + 2e^-$ ) on both the perfect and defect-containing graphene sheets. The calculations showed that the free energy ( $\Delta G$ ) of AA oxidation on the perfect and defect-containing graphene sheets was 1.82 and 1.36 eV at 0 V and pH of 0, which corresponded to the equilibrium reaction potential of AA oxidation vs Ag/AgCl electrode ( $E_{Ag/AgCl}^0$ ) at pH 7.4 being 150 mV (Figure 1G) and -80 mV (Figure 1H), respectively. A  $\sim 230$  mV overpotential was reduced for the defect-containing graphene sheet compared with the perfect

graphene sheet, agreeing with the experimental results for d-CNF-3 (Figure 1E). The varying equilibrium potential can be attributed to the enhanced adsorption energy of the dehydroascorbic acid (dhAA) on the defect-containing graphene sheet. Apparently, dhAA prefers to adsorb on the perfect graphene sheet with the lactone ring parallel to the graphene plane, whereas for the defect-containing graphene sheet, the dhAA molecules were vertically adsorbed on the surface with the carbonyl oxygen pointing toward the defect by forming hydrogen bonds. By performing Bader charge analyses, we found that  $\sim 0.2$  lel more electrons were transferred from the defect-containing graphene sheet to the dhAA compared with the perfect graphene sheet, leading to a lower overpotential and a higher current density for AA oxidation.

The oxygen levels were further controlled using two strategies. First, the power used during the oxygen plasma treatment was varied at 100, 200, or 400 W (denoted as o-CNF-1, o-CNF-2, and o-CNF-3). Second, the CNF was electrochemically polarized in 0.1 M NaOH and 0.5 M  $H_2SO_4$  (denoted as e-CNF). The oxygen levels were tracked by XPS. A typical XPS spectrum showed a C 1s peak at 285 eV and an O 1s peak at 531 eV (Figure S5). The d-CNF-3 was used as the control and exhibited a very weak O 1s peak, suggesting low oxygen levels of  $\sim 0.4\%$ . However, after the plasma power was increased, the corresponding oxidized CNFs exhibited higher oxygen levels (5.6% at 100 W, 10.9% at 300 W, and 11.8% at 400 W). Furthermore, higher oxygen levels of up to 12.6% were obtained after electrochemical treatment. High-resolution C 1s spectra were also used to analyze the oxygen-containing groups in as-prepared CNF, o-CNFs, and e-CNF (Figure 2A–C). The C 1s spectra of both o-CNFs and e-CNF showed a broader peak including four components located at 284.6, 286.2, 287.5, and 288.6 eV, which were attributed to C–C, C–O, C=O, and O=C–O, respectively.<sup>50</sup> Compared with o-CNFs and e-CNF, the C=O component was absent from the C 1s spectrum for CNF (Figure 2C,D), suggesting that the C=O group might play an important role in AA oxidation.

The electrochemical behavior of CNFs with different amounts of oxygen-containing groups was studied. The oxidation of AA was greatly enhanced for o-CNFs and e-CNF (Curve II in Figure 2E). On one hand, the overpotentials were more significantly reduced on CNF microelectrodes with oxygen-containing species (215 mV at o-CNF-1, 236 mV at o-CNF-2, 283 mV at o-CNF-3, and 227 mV at e-CNF) (Figure 2F).

On the other hand, the  $J_p$  values were much higher than that of the CNF and were further increased as the oxygen level increased. Compared with  $J_p$  value of CNF, the  $J_p$  was enhanced by 90% for o-CNF-1, 130% for o-CNF-2, 140% for o-CNF-3, and 170% for e-CNF. These results clearly demonstrated that the presence of oxygen-containing groups remarkably increased the electron transfer kinetics for AA oxidation. It is worth mentioning that the electrochemical treatment could clean and activate the electrode surface. In comparison to the raw CNF, the surface of MWCNTs in e-CNF became much rougher, the sidewalls of the MWCNTs were more bent and twisted, and more defects were produced in MWCNTs of CNF (Figure S4C). This structure was also beneficial for functionalization with oxygen-containing groups. Thus,  $J_p$  was enhanced more than that of o-CNFs. Surprisingly, a new oxidation peak at -270 mV was obtained for the e-CNF microelectrode (Curve I of Figure 2E), whereas no peak was observed for the as-prepared CNF or for the three types of o-CNFs. The new

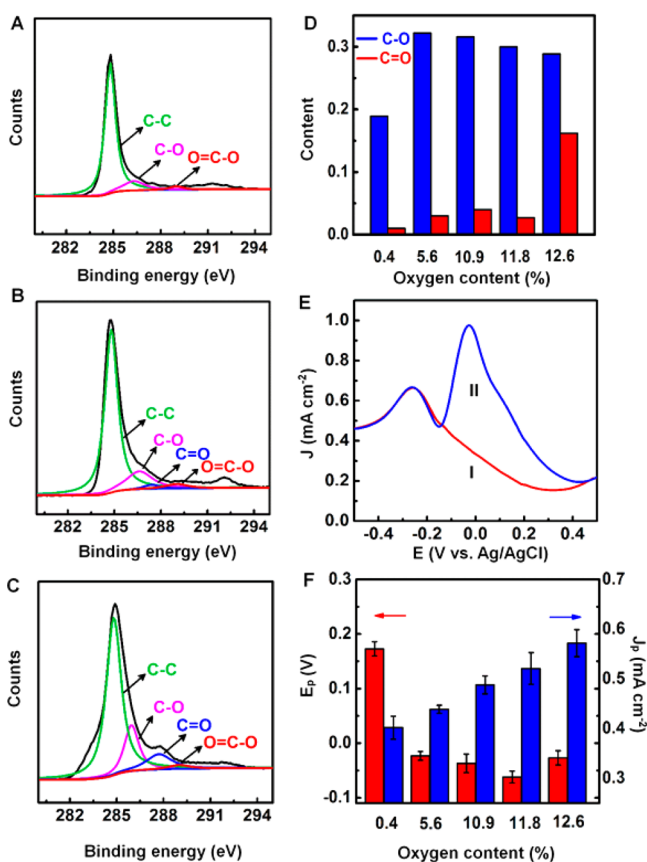


**Figure 2.** XPS C 1s spectra for the d-CNF-3 (A) and o-CNF-1 (B) or by e-CNF (C). (D) Comparison of the level of C–O and C=O components in d-CNF-3, the o-CNFs with different oxygen levels, and e-CNF with an oxygen level of 12.6%. (E) DPVs obtained from e-CNF in aCSF (pH 7.4) in the absence (I) or presence (II) of 0.5 mM AA. (F)  $E_p$  (red column) and  $J_p$  (blue column) of the AA oxidation peaks from the five microelectrodes in (D).

oxidation peak was completely separate from the anodic peak of AA (Curve II of Figure 2E), and its density remained unchanged as the AA concentration increased. Therefore, it can effectively serve as an internal reference to provide a built-in correction that avoids the environmental effects of the complex brain system. The new oxidation peak is related to the redox process of the quinone groups produced after electrochemical treatment. After CNF was pretreated by the electrochemical method, the C=O content clearly increased from <5% to ~16% (Figure 2D), indicating the inner reference was caused by the quinone groups in MWCNT. Furthermore, from Fourier transform infrared (FT-IR) spectra (Figure S6), we can see that the intensity of the peak in the region of 1650–1675  $\text{cm}^{-1}$  ascribed to the characteristic of C=O in quinone molecules markedly increased after electrochemical pretreatment of CNF, compared with that observed at CNF without pretreatment. The results are consistent with those obtained from XPS study, confirming that this inner reference peak was attributed to the redox process of quinone groups produced in carbon nanotubes after electrochemical treatment. Thus, the pH dependence of anodic peak current of inner reference was further determined in the pH range from 6.5 to 7.5 (Figure S7). A small deviation of peak current (<4.0%) indicates that the inner reference is still available for accurate detection of AA in brain environment with pH fluctuation, especially in the ischemia process.

The improved electron transfer and inherent oxidation peak that can serve as an internal reference make the e-CNF microelectrode a promising candidate for in vivo monitoring of AA levels. As demonstrated in Figure 3A, only one anodic peak

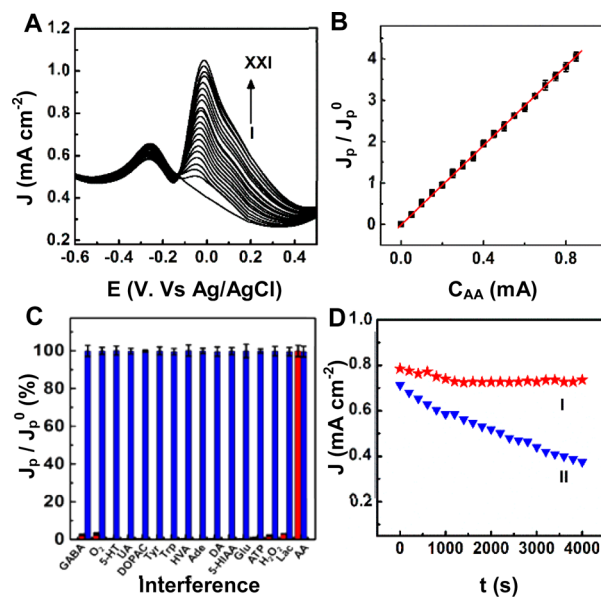


**Figure 3.** (A) DPVs obtained from an e-CNF in the aCSF solution containing increasing concentrations of AA from 0 to 1 mM (they are 0, 50, 100, 150, 200, 250, 300, 350, 400, 450, 500, 550, 600, 650, 700, 750, 800, 850, 900, 950, and 1000  $\mu\text{M}$  from I–XXI). (B) The linear plot between  $J_p/J_p^0$  and AA concentration. (C) Selectivity of the e-CNF microelectrodes toward potential interfering compounds in the rat brain. Their concentrations are 50 nM for GABA, 5-HT, Trp, Tyr, HVA, Ade, DA, and 5-HIAA; 0.2 mM for  $\text{O}_2$ ; 20  $\mu\text{M}$  for UA; 500 nM for DOPAC, ATP, and  $\text{H}_2\text{O}_2$ ; 5 mM for Glu and Lac; 200  $\mu\text{M}$  for AA. (D) Scanning stability test for the e-CNF microelectrode (I) and carbon fiber microelectrode (II) at  $-50$  mV in the aCSF solution (pH 7.4) over 4000 s.

located at  $-270$  mV was observed in the aCSF solution in the absence of AA. The  $J_p$  value of the anodic peak at  $-270$  mV was denoted as  $J_p^0$ . After 50  $\mu\text{M}$  AA was added to the aCSF solution, another oxidation peak appeared at  $-50$  mV which was attributed to the AA oxidation process. In addition, the  $J_p$  value of this anodic peak gradually increased as the AA concentration increased. The ratiometric peak current density ( $J_p/J_p^0$ ) was linear to the AA concentration in the range of 50  $\mu\text{M}$  to 1 mM (Figure 3B). The detection limit was as low as 10  $\mu\text{M}$ , with a sensitivity of 0.85  $\text{mA mol}^{-1} \text{cm}^{-2}$ . The current e-CNF-based microsensors demonstrated a low working potential, wide linear range, and high sensitivity.<sup>31,32,51,52</sup>

The low overpotential for AA oxidation at the pretreated CNF microelectrode is critical for determining AA levels with high selectivity in cerebral systems. As summarized in Figure 3C, no obvious responses (<2.0%) were observed upon the addition of neurotransmitters and other potential interfering compounds. Particularly for electroactive neurotransmitters including 5-HT, UA, DOPAC, and DA, their potentials were more positive than and well separated from that of AA even in mixed solution with all molecules (Figure S8), suggesting our electrode possessed good resistance toward these neurochemicals. In addition, only slight changes (<1.0%) were observed for the competition test. These results established the basis of in vivo selective measurement of AA in living brains

with the developed ratiometric electrochemical sensor. Furthermore, the e-CNF-based microsensor possessed good resistance against electrode fouling even after continuously scanning for 1000 cycles (Figure S9). More importantly, a slight decrease of 1.8% in current density was observed after measuring AA for 4000 s, demonstrating a high scanning stability (Figure 3D). In order to evaluate the antibiofouling ability of e-CNF microelectrode for AA determination in rat brains, we recorded  $J_p/J_p^0$  values in aCSF (pH 7.4) containing 4% BSA and 500  $\mu\text{M}$  AA. A small deviation (<6%) of  $J_p/J_p^0$  during a 2 h determination indicates good antibiofouling ability of the present e-CNF microelectrode (Figure S10). In addition, the deviation of the  $J_p/J_p^0$  of 6 sensors prepared with the same method did not exceed 3.8% (S.D.,  $n = 6$ ), indicating good reproducibility of the present CNF microelectrode (Figure S11).

In combination with high performance properties, the e-CNF can be effectively used for the monitoring of AA levels in the brain. The e-CNF was used to detect AA in vivo in a living rat brain (Figure 4A,B). Figure 4C shows the electrochemical

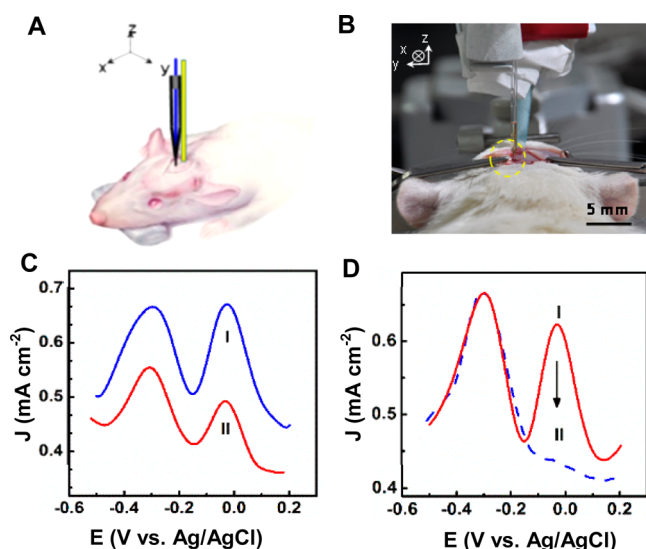


**Figure 4.** (A) Schematic illustration of the in vivo setup for determining AA in rat brain. (B) Optical images before and after the stereotaxic implant into the brain. (C) DPVs recorded at the e-CNF microelectrode in the striatum of normal rat (I) and rat brain models of AD (II). (D) DPV responses recorded at the e-CNF microelectrode in the striatum of the rat brain model of AD before (I) and after (II) injection of AAox.

responses obtained by the ratiometric microsensor in normal rat brain (Curve I) and in a rat brain model of AD (Curve II). Two separate oxidation peaks were clearly observed at approximately  $-290$  and  $-60$  mV at the e-CNF microelectrode in the normal rat brain, whereas only one peak was obtained at  $-290$  mV in pure aCSF, suggesting that AA was present in the rat brain. Furthermore,  $J_p$  of the peak located at a more positive potential obviously decreased in the rat brain model of AD, indicating a marked decrease in AA concentration (Curve II of Figure 4C). The slight potential shift was caused by an outer reference shift during the in vivo experiment. The peak located at  $-60$  mV disappeared after exogenous infusion of AAox, an AA scavenger, while the peak at  $-290$  mV remained constant (Figure 4D). As a control, pure aCSF (pH 7.4) was microinjected into the brain for 15 min. However, the infusion

of aCSF only gave rise to a slight decrease of AA oxidation current (<5%) (Figure S12). These results demonstrated that the peak located at  $-60$  mV resulted from the AA oxidation. Five e-CNF microelectrodes were tested in similar conditions (Figure S13). The small deviation (<4%) demonstrates the present electrode possesses good electrode-to-electrode reproducibility. The basal concentrations of AA in the normal rat brains were estimated to be  $259 \pm 6 \mu\text{M}$  in cortex,  $264 \pm 20 \mu\text{M}$  in striatum, and  $261 \pm 21 \mu\text{M}$  in hippocampus on average ( $n = 3$ ), respectively. However, the overall AA level exhibits a downward trend in rat brain models of AD. The AA concentration was decreased to  $210 \pm 30 \mu\text{M}$  in cortex,  $182 \pm 5 \mu\text{M}$  in striatum, and  $136 \pm 20 \mu\text{M}$  in hippocampus (Table S1). These quantitative characterizations of AA concentration in the rat brain model of AD have not been previously reported.

We also applied this ratiometric electrochemical microsensor to the real-time monitoring of AA in three brain regions at different times following global cerebral ischemia (Figure S14). Surprisingly, the concentration of AA increased by ca. 2.0-fold in the hippocampus and ca. 3.9-fold in the cortex within 30 min. However, a negligible change in AA concentration was observed in the striatum region of the rat brain upon global cerebral ischemia, even for 1 h. These results are consistent with previous reports.<sup>10,53</sup> However, to the best of our knowledge, those opposite AA alternations in rat brains between AD and ischemia have never been reported.

## CONCLUSIONS

In summary, the functional CNFs with tunable defects and oxygen-containing groups were discovered to act as an accurate and selective microsensor for the ratiometric detection of AA levels in the brain model of AD rat. The engineered defects and functional groups on the CNF play a vital role in the electrocatalytic activity for AA oxidation at low potentials, resulting in high selectivity toward AA over other potential interfering compounds in the brain. More interestingly, a new peak appears for the CNF and remained constant as the AA concentration changed, offering an effective internal reference to improve detection accuracy. On the basis of the unique properties of CNFs, we established an accurate and selective platform for in vivo monitoring of AA concentrations in the brain of AD rat. This work also provides a methodology for designing and constructing high-performance biosensors for other neurotransmitters and might encourage new directions in brain chemistry research.

## ASSOCIATED CONTENT

### Supporting Information

The Supporting Information is available free of charge on the ACS Publications website at DOI: 10.1021/acs.analchem.6b04168.

The establishment of AD rat model; TEM images of as-purified MWCNTs and MWCNT with amorphous carbon; CVs obtained at CNF microelectrodes in the presence of  $\text{Fe}(\text{CN})_6^{3-}$ ; typical Raman spectra of CNF and d-CNF obtained at 200 °C; TEM images of MWCNTs in d-CNFs after a heating treatment at 300 and 400 °C; XPS spectra of MWCNTs in various CNFs; FT-IR spectra recorded at as-prepared CNF and e-CNF; pH dependence of  $J_p^0$  values; selectivity for AA toward electroactive neurochemicals; stability of e-CNF microelectrode; antibiofouling ability of the e-CNF micro-

electrode; reproducibility; the concentrations of AA determined in three regions of normal rat brains and rat brains with AD by the present method; DPVs comparison for AA oxidation in rat brain before and after microinjection of aCSF; the electrode-to-electrode reproducibility; AA concentrations in rat brains followed by ischemia under different times (PDF)

## AUTHOR INFORMATION

### Corresponding Authors

\*Phone: + 86 21 54341041. Fax: +86 21 54341041. E-mail: [ytian@chem.ecnu.edu.cn](mailto:ytian@chem.ecnu.edu.cn).

\*Phone: + 86 21 65642400. Fax: +86 21 65642400. E-mail: [zpliu@fudan.edu.cn](mailto:zpliu@fudan.edu.cn).

\*Phone: + 86 21 51630316. Fax: +86 21 51630316. E-mail: [penghs@fudan.edu.cn](mailto:penghs@fudan.edu.cn).

### ORCID

Yang Tian: 0000-0001-8850-0349

### Author Contributions

<sup>‡</sup>L.Z. and F.L. equally contributed to this work.

### Notes

The authors declare no competing financial interest.

## ACKNOWLEDGMENTS

This work was financially supported by NSFC (21635003 for Y.T.; 21305104, 21545002, and 21675054 for L.Z.) and National Nature Science Fund for distinguished Yong Scholars (21325521 for Y.T.).

## REFERENCES

- (1) Tsukaguchi, H.; Tokui, T.; MacKenzie, B.; Berger, U.; Chen, X.; Wang, Y.; Brubaker, R.; Hediger, M. *Nature* **1999**, *399*, 70.
- (2) Harrison, F.; May, J. *Free Radical Biol. Med.* **2009**, *46*, 719.
- (3) May, J.; Qu, Z.; Mendiratta, S. *Arch. Biochem. Biophys.* **1998**, *349*, 281.
- (4) Kontos, H. *Stroke* **2001**, *32*, 2712.
- (5) Rebec, G.; Barton, S.; Marseilles, A.; Collins, K. *NeuroReport* **2003**, *14*, 1263.
- (6) Nagayama, H.; Hamamoto, M.; Ueda, M.; Nito, C.; Yamaguchi, H.; Katayama, Y. *Clin. Neuropharmacol.* **2004**, *27*, 270.
- (7) Dorner, J.; et al. *Brain Res.* **2009**, *1290*, 111.
- (8) Acuna, A.; Esparza, M.; Kramm, C.; Beltran, F.; Parra, A.; Cepeda, C.; Toro, C.; Vidal, R.; Hetz, C.; Concha, I.; Brauchi, S.; Levine, M.; Castro, M. *Nat. Commun.* **2013**, *4*, 1.
- (9) Crespi, F. *Neurosci. Lett.* **1996**, *215*, 189.
- (10) Liu, K.; Lin, Y.; Yu, P.; Mao, L. *Brain Res.* **2009**, *1253*, 161.
- (11) Sotiriou, S.; Gispert, S.; Cheng, J.; Wang, Y.; Chen, A.; Hoogstraten-Miller, S.; Miller, G.; Kwon, O.; Levine, M.; Guttentag, S.; Nussbaum, R. *Nat. Med.* **2002**, *8*, 514.
- (12) Deakin, M.; Kovach, P.; Stutts, K.; Wightman, R. *Anal. Chem.* **1986**, *58*, 1474.
- (13) Gardiner, T.; Armstrong-James, M.; Cans, A.; Wightman, R. M.; Rebec, G. *Brain Res.* **1985**, *344*, 181.
- (14) Francois, J.; Huxter, J.; Conway, M. W.; Lowry, J. P.; Tricklebank, M. D.; Gilmour, G. J. *J. Neurosci.* **2014**, *34*, 596.
- (15) Phillips, P.; Stuber, G.; Heien, M.; Wightman, R.; Carelli, R. *Nature* **2003**, *422*, 614.
- (16) Thompson, J.; Peterson, M.; Freeman, R. *Science* **2003**, *299*, 1070.
- (17) Robinson, D.; Hermans, A.; Seipel, A.; Wightman, R. M. *Chem. Rev.* **2008**, *108*, 2554.
- (18) Luo, Y.; Zhang, L.; Liu, W.; Yu, Y.; Tian, Y. *Angew. Chem., Int. Ed.* **2015**, *54*, 14053.
- (19) Chai, X.; Zhou, X.; Zhu, A.; Zhang, L.; Qin, Y.; Shi, G.; Tian, Y. *Angew. Chem., Int. Ed.* **2013**, *52*, 8129.

- (20) Zhou, J.; Zhang, L.; Tian, T. *Anal. Chem.* **2016**, *88*, 2113.
- (21) Zhao, F.; Zhang, L.; Zhu, A.; Shi, G.; Tian, T. *Chem. Commun.* **2016**, *52*, 3717.
- (22) Ewing, A.; Alloway, K.; Curtis, S.; Dayton, M.; Wightman, R.; Rebec, R. *Brain Res.* **1983**, *261*, 101.
- (23) Gu, H.; Varner, E.; Groskreutz, S.; Michael, A.; Weber, S. *Anal. Chem.* **2015**, *87*, 6088.
- (24) Kato, D.; Goto, K.; Fujii, S.; Takatsu, A.; Hirono, S.; Niwa, O. *Anal. Chem.* **2011**, *83*, 7595.
- (25) Dunevall, J.; Fathali, H.; Najafinobar, N.; Lovric, J.; Wigstrom, J.; Cans, A.; Ewing, A. J. *Am. Chem. Soc.* **2015**, *137*, 4344.
- (26) McCreery, R. In *Electroanalytical Chemistry*; Dekker: New York, 1991; p 221.
- (27) Gong, K.; Chakrabarti, S.; Dai, L. *Angew. Chem., Int. Ed.* **2008**, *47*, 5446.
- (28) Yang, W.; Ratnac, K.; Ringer, S.; Thordarson, P.; Gooding, J.; Braet, F. *Angew. Chem., Int. Ed.* **2010**, *49*, 2114.
- (29) Luo, H.; Shi, Z.; Li, N.; Gu, Z.; Zhuang, Q. *Anal. Chem.* **2001**, *73*, 915.
- (30) McCreery, R. *Chem. Rev.* **2008**, *108*, 2646.
- (31) Zhang, M.; Liu, K.; Xiang, L.; Lin, Y.; Su, L.; Mao, L. *Anal. Chem.* **2007**, *79*, 6559.
- (32) Xiang, L.; Yu, P.; Hao, J.; Zhang, M.; Zhu, L.; Dai, L.; Mao, L. *Anal. Chem.* **2014**, *86*, 3909.
- (33) Chen, P.; Xu, Y.; He, S.; Sun, X.; Pan, S.; Deng, J.; Chen, D.; Peng, H. *Nat. Nanotechnol.* **2015**, *10*, 1077.
- (34) Zhang, Z.; Guo, K.; Li, Y.; Li, X.; Guan, G.; Li, H.; Luo, Y.; Zhao, F.; Zhang, Q.; Wei, B.; Pei, Q.; Peng, H. *Nat. Photonics* **2015**, *9*, 233.
- (35) Sun, X.; Chen, T.; Yang, Z.; Peng, H. *Acc. Chem. Res.* **2013**, *46*, 539.
- (36) Vigolo, B.; Penicaud, A.; Coulon, C.; Sauder, C.; Paillet, R.; Journet, C.; Bernier, P.; Poulin, P. *Science* **2000**, *290*, 1331.
- (37) Harreither, W.; Trouillon, R.; Poulin, P.; Neri, W.; Ewing, A. G.; Safina, G. *Anal. Chem.* **2013**, *85*, 7447.
- (38) Schmidt, A. C.; Wang, X.; Zhu, Y.; Sombers, L. A. *ACS Nano* **2013**, *7*, 7864.
- (39) Chen, T.; Cai, Z.; Yang, Z.; Li, L.; Sun, X.; Huang, T.; Yu, A.; Kia, H.; Peng, H. *Adv. Mater.* **2011**, *23*, 4620.
- (40) Guo, W.; Liu, C.; Zhao, F.; Sun, X.; Yang, Z.; Chen, T.; Chen, X.; Qiu, L.; Hu, X.; Peng, H. *Adv. Mater.* **2012**, *24*, 5379.
- (41) Fang, Y.; Liu, Z. *J. Am. Chem. Soc.* **2010**, *132*, 18214.
- (42) Wei, G.; Fang, Y.; Liu, Z. *J. Phys. Chem. C* **2012**, *116*, 12696.
- (43) Bockris, J. O'M.; Khan, S. U. M. *Surface Electrochemistry*; Plenum Press: New York, 1993.
- (44) Rossmel, J.; Logadottir, A.; Nørskov, J. K. *Chem. Phys.* **2005**, *319*, 178.
- (45) Yu, Y.; Zhang, L.; Li, C.; Sun, X.; Tang, D.; Shi, G. *Angew. Chem., Int. Ed.* **2014**, *53*, 12832.
- (46) De Butte, M.; Fortin, T.; Pappas, B. *Neurobiol. Aging* **2002**, *23*, 309.
- (47) Yonekura, I.; Kawahara, N.; Nakatomi, H.; Furuya, K.; Kirino, T. *J. Cereb. Blood Flow Metab.* **2004**, *24*, 151.
- (48) Luo, H.; Shi, Z.; Li, N.; Gu, Z.; Zhuang, Q. *Anal. Chem.* **2001**, *73*, 915.
- (49) Li, H.; Sun, X.; Peng, H. *ChemPhysChem* **2015**, *16*, 3761.
- (50) Kovtyukhova, N.; Mallouk, T.; Pan, L.; Dickey, E. J. *Am. Chem. Soc.* **2003**, *125*, 9761.
- (51) Ferreira, N.; Santos, R.; Laranjinha, J.; Barbosa, R. *Electroanalysis* **2013**, *25*, 1757.
- (52) Cheng, H.; Wang, X.; Wei, H. *Anal. Chem.* **2015**, *87*, 8889.
- (53) Liu, K.; Lin, Y.; Xiang, L.; Yu, P.; Su, L.; Mao, L. *Neurochem. Int.* **2008**, *52*, 1247.